Cement and Concrete Research 163 (2023) 107014

Contents lists available at ScienceDirect

Cement and Concrete Research

journal homepage: www.elsevier.com/locate/cemconres

Thermally activated viscoelasticity of cement paste: Minute-long creep tests and micromechanical link to molecular properties

Eva Binder [a,b,d,1], Markus Königsberger [a,c,1], Rodrigo Díaz Flores [a], Herbert A. Mang [a,d], Christian Hellmich [a], Bernhard L.A. Pichler [a,*]

[a] TU Wien (Vienna University of Technology), Karlsplatz 13/202, 1040 Vienna, Austria
[b] Linnaeus University, Universitetsplatsen 1, 35195, Växjö, Sweden
[c] ULB (Université libre de Bruxelles), Avenue Franklin Roosevelt 50, 1050 Brussels, Belgium
[d] College of Civil Engineering, Tongji University, 1239 Siping Road, Shanghai, China

ARTICLE INFO

Keywords:
Creep testing
Multiscale modeling
Creep modulus
Elastic modulus
Thermal activation
Activation energy

ABSTRACT

The stiffness of cementitious materials decreases with increasing temperature. Herein, macroscopic samples of mature cement pastes are subjected at 20, 30, and 45 °C, respectively, to three-minutes-long creep compression experiments. The test evaluation is based on the linear theory of viscoelasticity and Boltzmann's superposition principle. This yields macroscopic elastic and creep moduli as a function of temperature. A state-of-the-art multiscale model for creep homogenization of cement paste is extended to account for temperature-dependent elastic and creep moduli of the hydrate gel. This extension is based on results from published molecular simulations. Temperature-independent stiffness is assumed for cement clinker. Upscaling to the macroscale of cement paste yields elastic and creep moduli which agree well with the aforementioned experimental results. The Arrhenius-type activation energy of the creep modulus is found to be independent of scale, composition, and maturity, because of ineffective stress redistributions from creeping to non-creeping constituents.

1. Introduction

Stiffness of concrete, i.e. the mechanical stresses needed per deformation unit of the loaded material, is known to decrease with increasing temperature. This refers to both the instantaneous elastic stiffness [1,2], associated with zero dissipation [3], and to the delayed diminishing stiffness, standardly referred to as relaxation (under constant strain) or creep (under constant stress) [4–9]. Restricting the discussion to representative service conditions in civil engineering, say up to 50 centigrades, the former, instantaneously elastic effect does not exceed a few percent [1,2], while the latter, i.e. the relaxation-related effect may entail a stiffness reduction of virtually two [4–9]. The creep stiffness reduction is typically captured by means of an Arrhenius-type activation law, with the corresponding activation energies known to be close to that of water [9,10]. This indicates that nanoscopic processes involving confined water are essential for the macroscopic response of the material [11–13].

The present study aims at providing a precise experimental and theoretical link between the effect of temperature on the elastic and creep stiffness at the molecular scale, as recently deciphered by a series of molecular dynamics studies [14–19], and the macroscopic scale of cement paste samples. Therefore, disturbing effects resulting from ongoing hydration or cracking, as often encountered during characteristic time and loading regimes of conventional creep tests, are minimized. More precisely, an experimental setup is used, which is based on creep tests under uniaxial compression, lasting for three minutes [20–23]: This setup gives direct access to the elastic and the creep response of samples at a constant degree of hydration. They are only subjected to mild loading, exceeding not more than 20% of the material strength. As regards theory and material modeling, a state-of-the-art continuum micromechanics model [24,25] is employed in order to provide a scale bridge between latter macroscopic tests and former molecular dynamics modeling results. It will allow for casting well-known trends between stiffness and temperature into quantitative relations with a clear chemo-physical meaning.

Accordingly, the paper is organized as follows: Section 2 deals with the isothermal short-term creep tests. Section 3 is devoted to micro-to-macro upscaling of temperature-dependent viscoelastic properties

* Corresponding author.
E-mail addresses: Eva.Binder@tuwien.ac.at (E. Binder), Markus.Konigsberger@ulb.be (M. Königsberger), Rodrigo.Diaz@tuwien.ac.at (R. Díaz Flores), Herbert.Mang@tuwien.ac.at (H.A. Mang), Christian.Hellmich@tuwien.ac.at (C. Hellmich), Bernhard.Pichler@tuwien.ac.at (B.L.A. Pichler).
URL: http://www.imws.tuwien.ac.at (B.L.A. Pichler).
[1] Authors have contributed equally.

https://doi.org/10.1016/j.cemconres.2022.107014
Received 23 December 2021; Received in revised form 3 October 2022; Accepted 22 October 2022
Available online 17 November 2022

Table 1
Mass, height, and diameter of five specimens made of cement paste with $w/c = 0.42$, three months after production.

specimen ID	mass [g]	height [mm]	diameter [mm]
1	2450	309.3	70.93
2	2372	300.1	70.70
3	2358	298.4	70.38
4	2324	283.4	70.96
5	2340	295.2	70.81

and to a comparison of model predictions with experimental results. Section 4 contains a discussion regarding the origin of the macroscopic activation energy associated with the temperature-dependence of the creep modulus. Section 5 contains the conclusions drawn from the results of the present study.

2. Three-minutes creep tests under uniaxial compression

As for the present study, five cylinders of cement paste were produced (nominal height and diameter amounted to 300 mm and 70 mm, respectively). Each one of them was tested at three different temperatures, resulting in a total of 15 individual tests. The specimens were produced in three batches, using the same raw materials. A commercial cement of type CEM I 42.5 N was mixed with distilled water. The initial water-to-cement mass ratio, w/c, amounted to 0.42. The molds containing the freshly-mixed material were sealed and stored in a climatic chamber at 20 °C. One day later, the specimens were taken out of the molds. For the following three months, they were stored in lime-saturated water at 20 °C. Before testing, the mass m, the height h, and the diameter d of the specimens were measured, see Table 1.

2.1. Test setup, protocol, and results

In order to prepare the specimens for testing at different temperatures, they were stored for at least 20 h in lime-saturated water, tempered at the testing temperature of either 20, 30, or 45 °C. Thereafter, the samples were taken out of the water. They were covered by several layers of food preservation foil to avoid significant loss of water during subsequent creep testing.

The experimental setup was equal to the one developed in the context of early-age characterization of cement pastes [26,27], mortars [20], and concretes [20,22]. The tests were performed inside a thermally insulated chamber equipped with a temperature control unit "Lauda RK8 KP". The chamber was integrated into an electromechanical testing machine of type "Zwick-Roell Z050". The specimens were placed in between two metal cylinders equipped with so-called bottlenecks, see Fig. 1. This allowed for fine-tuning the position of the specimens, such that they were subjected, in a close-to-perfect fashion, to uniaxial compression, see [26,27] for details. Loading was carried out under force-control, using the load cell integrated into the testing machine. The deformations of the specimens were recorded by means of five Linear Variable Displacement Transducers (LVDTs) of type "HBM W1/2 mm-T". Equally distributed around the specimen, they measured the relative displacement between two aluminum rings. The latter were fixed to the cylindrical specimens at a distance of some 70 mm from their top and bottom surfaces. The initial distance between the two rings, referred to as the measurement length, amounted to 164 mm. This central measurement region is practically free of undesired shear stresses, see Fig. 2 of [26].

The normal stress component, σ, and the normal strain component, ε, both in the loading direction, are quantified as follows. The stress history, $\sigma(t)$, is obtained by dividing the prescribed force history, $F(t)$, by the cross-sectional area $A = d^2\pi/4$ of the specimens, i.e.

$$\sigma(t) = \frac{F(t)}{A}, \tag{1}$$

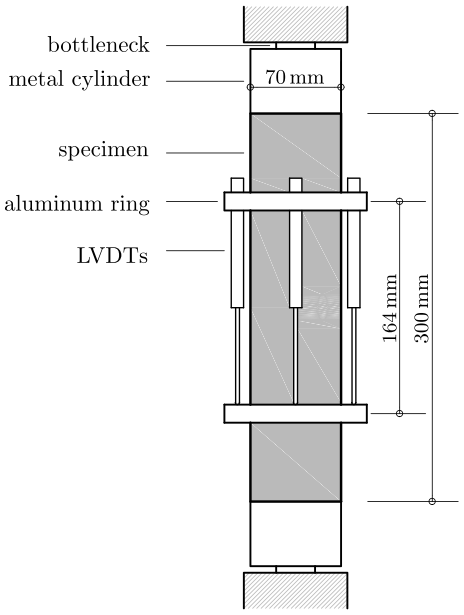

Fig. 1. Test setup consisting of a cement paste sample, metal cylinders with bottlenecks, and two aluminum rings holding five Linear Variable Displacement Transducers (LVDTs), equally distributed around the specimen [20].

where t denotes the time. The strain histories, $\varepsilon(t)$, follow from dividing the average of the changes of length measured by the five LVDTs, $\Delta\ell_i(t)$, with $i = 1, 2, 3, 4, 5$, by the measurement length given as 164 mm, i.e.

$$\varepsilon(t) = \left[\frac{1}{5}\sum_{i=1}^{5}\Delta\ell_i(t)\right] \times \frac{1}{164\,\text{mm}}. \tag{2}$$

The following test protocol was used. Each specimen was placed inside the thermally insulated chamber that was adjusted to the desired testing temperature. The position of the specimens was fine-tuned. Thereafter, the specimens were subjected to a small compressive force, equal to 0.2 kN. This ensured good contact between the specimens and the load application system. The specimens remained in this configuration for at least 12 h. This ensured that the contribution of the time-dependent deformations of the specimens, resulting from the small permanent load, to the deformations measured during the actual creep tests was negligible. In these tests, the stress was increased with a speed of 2 MPa/s up to 12 MPa. This is expected to be 15% of the quasi-static uniaxial compressive strength of the material at the time of testing [28,29]. This stress level was kept constant for three minutes, see Fig. 2. On the one hand, the chosen load level is large enough to obtain reliable deformation measurements. On the other hand, it is small enough to ensure that the material is not damaged during the test [30], and that testing is performed in the linear creep regime [31]. Therefore, the creep-testing-induced deformations of the specimens were fully recoverable, see Fig. 18 of [27] for a comparable situation. The recovery time allotted to every specimen between subsequent creep tests was by far longer than the duration of the creep experiments. Thus, also the second and the third creep test performed on the same specimen were started from a fully recovered configuration. Therefore, each creep experiment was independent of others, performed on the same specimen.

The strain histories measured during testing of each one of the five specimens at the three different temperatures are the central result of the testing campaign. The repeatability of the tests is satisfactory, because the graphs of the five strain histories, measured at the same temperature, are rather close to each other, see the black solid lines in Fig. 3. Comparing experimental results obtained with different temperatures, underlines that the measured strains are the larger, the higher the temperature.

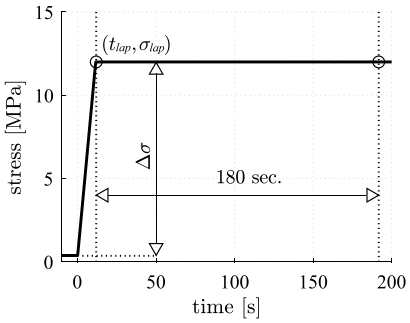

Fig. 2. Stress history prescribed in the context of three-minutes creep tests: t_{lap} and σ_{lap} label the end of the load application process.

2.2. Quantification of the elastic modulus and the creep modulus

The described creep experiments are evaluated in the framework of the linear theory of viscoelasticity [32]. Boltzmann's superposition principle [33] is used to relate the prescribed stress history $\sigma(t)$, see Fig. 2, to the measured strain evolutions $\varepsilon(t)$, see Fig. 3. This yields the following convolution integral

$$\varepsilon(t) = \int_0^t J(t-\tau)\,\frac{\partial\sigma}{\partial\tau}\,\mathrm{d}\tau\,, \tag{3}$$

where $J(t-\tau)$ denotes the uniaxial creep function, $\partial\sigma/\partial\tau$ stands for the stress rate, and τ denotes the time-like integration variable. A power-law type creep function is used, as proposed by Tamtsia and Beaudoin [34]. Such a creep function was successfully applied to repeated minute-long creep tests on hydrating cement pastes [27], mortars [20], and concretes [22]. Denoting the elastic modulus as E_e, the creep modulus as E_c, the power-law exponent as β, and the reference time as t_{ref}, the modeled creep function reads as [27]:

$$J(t-\tau) = \frac{1}{E_e} + \frac{1}{E_c}\left(\frac{t-\tau}{t_{ref}}\right)^{\beta}. \tag{4}$$

The first term on the right-hand-side of Eq. (4) refers to the *elastic* compliance of the material. It is associated with instantaneous (= "time-independent") deformations which are non-dissipative and reversible. The second term refers to the *creep* compliance. It is associated with delayed (= "time-dependent") deformations which are still reversible, albeit not instantaneously, but dissipative. The corresponding thermodynamic situation is the following [35, pages 264f]. At instantaneous unloading of a sample, the elastic deformation is immediately recovered, performing work on the sample's surroundings (i.e. on the testing machine), while the creep deformation does not show an immediate change. However, the energy trapped inside the sample in terms of microelastic deformations, starts to trigger viscous processes within the sample's microstructure. With growing time, this leads to full recovery of the creep deformations. For this to happen, the aforementioned trapped energy is "consumed" by dissipation into heat.

The prescribed stress history of Fig. 2 is a bilinear function with piecewise constant stress rates:

$$\frac{\partial\sigma}{\partial\tau} = \begin{cases} \dot\sigma = \text{const.} & 0 \le t \le t_{lap}\,, \\ 0 & t > t_{lap}\,. \end{cases} \tag{5}$$

Inserting Eqs. (4) and (5) into Eq. (3) yields a piecewise analytical solution for the strains [22]:

$$\varepsilon(t) = \frac{\dot\sigma\, t}{E_e} + \frac{\dot\sigma\, t_{ref}}{E_c\,(\beta+1)}\left(\frac{t}{t_{ref}}\right)^{\beta+1}, \qquad 0 \le t \le t_{lap}\,, \tag{6}$$

$$\varepsilon(t) = \frac{\dot\sigma\, t_{lap}}{E_e} + \frac{\dot\sigma\, t_{ref}}{E_c\,(\beta+1)}\left[\left(\frac{t}{t_{ref}}\right)^{\beta+1} - \left(\frac{t-t_{lap}}{t_{ref}}\right)^{\beta+1}\right], \quad t \ge t_{lap}\,. \tag{7}$$

Table 2
Values of the elastic modulus E_e and the creep modulus E_c identified at the three investigated temperatures, and statistical values: arithmetic mean values, standard deviations, m-parameters and s-parameters of log-normal distributions, see Eq. (9), and quantiles according to Eq. (10).

Experimental data						
Temperature:	20 °C		30 °C		45 °C	
Specimen ID	E_e [GPa]	E_c [GPa]	E_e [GPa]	E_c [GPa]	E_e [GPa]	E_c [GPa]
1	21.2	40.8	21.3	32.3	20.4	20.0
2	21.4	40.4	20.8	30.3	20.5	19.6
3	20.8	50.5	21.1	43.3	20.1	28.3
4	20.9	36.0	21.2	31.1	20.9	22.9
5	21.8	40.2	20.8	35.6	20.6	23.9
Statistical analysis						
Arithmetic mean [GPa]:	21.3	41.6	21.0	34.6	20.5	22.9
Standard deviation [GPa]:	0.4	5.4	0.2	5.3	0.3	3.5
m – parameter [log(MPa)]:	9.9643	10.6294	9.9533	10.4408	9.9275	10.0309
s – parameter [log(MPa)]:	0.0190	0.1227	0.0083	0.1454	0.0150	0.1486
2.5%-quantile [GPa]:	20.48	32.50	20.68	25.74	19.90	16.98
97.5%-quantile [GPa]:	22.06	52.57	21.37	45.52	21.10	30.40

One central aim of the present contribution is to raise awareness that deformations of cementitious materials, resulting from short loading phases, contain both elastic *and* creep contributions. This provides the motivation to evaluate Eq. (6) for the end of the load application process, i.e. for $t = t_{lap}$:

$$\varepsilon(t_{lap}) = \frac{\dot\sigma\, t_{lap}}{E_e} + \frac{\dot\sigma\, t_{ref}}{E_c\,(\beta+1)}\left(\frac{t_{lap}}{t_{ref}}\right)^{\beta+1}. \tag{8}$$

Eq. (8) emphasizes that the strains, measured during a loading process, contain "elastic" and "creep" contributions. It is important to consider this fact when quantifying the elastic modulus E_e and the creep modulus E_c based on the results of creep tests.

As for three-minutes creep tests of cementitious materials, the reference time is commonly set equal to one day, $t_{ref} = 86400$ s [20,22,24,27,36,37]. The power-law exponent β is assumed to be constant in the investigated temperature range. It is set equal to 0.25 [22,24,36,37]. In the present study, the stress rate during loading, $\dot\sigma$, is equal to 2 MPa/s. Thus, there are only two remaining unknowns in Eqs. (6) and (7): the elastic modulus E_e and the creep modulus E_c. They are identified such that the squared differences between the output of Eqs. (6) and (7) and the measured strains illustrated in Fig. 3 become a minimum. The analysis is done iteratively, with progressively refined search grids [27]. The described identification procedure is applied to each one of the 15 measured strain evolutions. This results in 15 pairs of values of E_e and E_c, see Table 2 and Appendix B. With increasing temperature, the modulus of elasticity decreases slightly, whereas the creep modulus decreases significantly, see Fig. 4.

2.3. Statistical analysis

The statistical analysis of the identified moduli is based on log-normal distributions [38]. They take into account that stiffness moduli are positive quantities. The probability density function (PDF) of the log-normal distribution reads as

$$PDF(E_i) = \frac{1}{E_i\, s_i \sqrt{2\pi}}\,\exp\left[-\frac{\left(\log E_i - m_i\right)^2}{2 s_i^2}\right], \qquad i \in \{e,\, c\}\,, \tag{9}$$

where E_i represents the statistical variable, i.e. either the elastic modulus ($i = e$) or the creep modulus ($i = c$). The symbols m_i and s_i denote the expected value and the standard deviation, respectively, of the natural logarithm of the moduli. They are quantified with Matlab for the statistical samples of the elastic and creep moduli, obtained at 20, 30, and 45 °C, respectively, see Table 2. The identified values of m_i

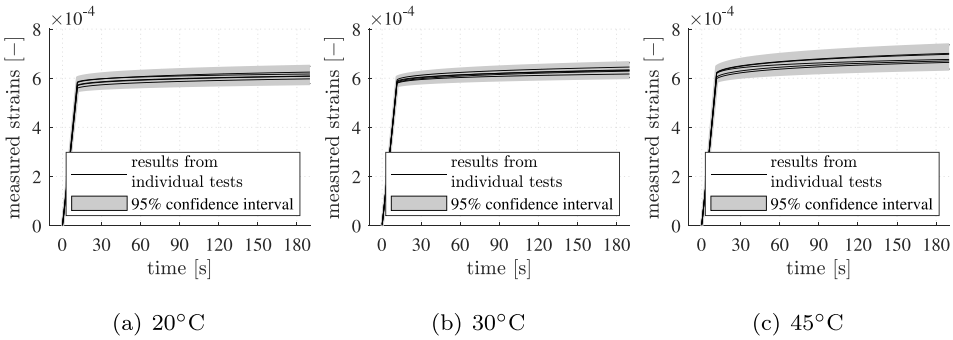

Fig. 3. Strain histories measured during three-minutes creep tests of five different specimens, carried out at three different temperatures: the black solid lines refer to measurements obtained from testing of individual specimens, the gray area represents the 95% confidence interval of the strains, estimated by means of log-normal distributions of the elastic modulus and the creep modulus, respectively. (For interpretation of the references to color in this figure legend, the reader is referred to the web version of this article.)

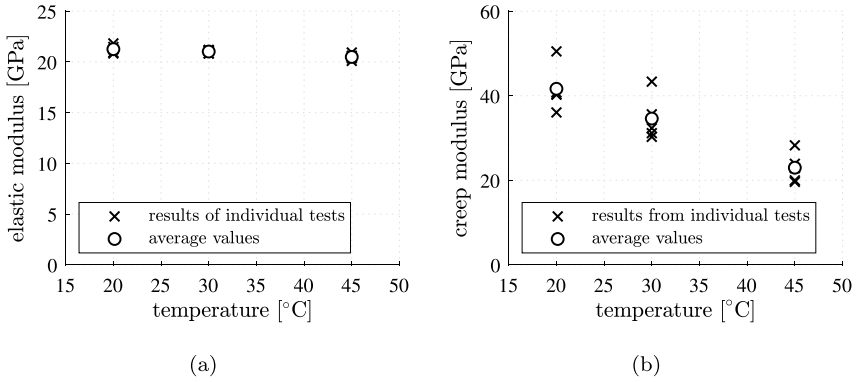

Fig. 4. Identified values of (a) the elastic modulus, E_e, and (b) the creep modulus, E_c, as functions of the testing temperature: the crosses refer to results from individual tests, the circles to mean values of results from five tests performed at the same temperature.

and s_i are the basis for quantifying the 2.5% and the 97.5% quantiles of the moduli as

$$E_i(P) = \exp\left[m_i + s_i\,\sqrt{2}\,\mathrm{erf}^{-1}\,(2P-1)\right], \qquad \begin{cases} i \in \{e,\,c\}\,, \\ P \in \{0.025,\,0.975\}\,. \end{cases} \tag{10}$$

Based on the quantiles, 95% confidence intervals for the strains are computed. The lower boundaries of the gray areas in Fig. 3 refer to total strains, calculated with the 97.5% quantiles of the elastic and creep moduli. The upper boundaries refer to the 2.5% quantiles.

3. Multiscale modeling

A continuum micromechanics model is used to describe the macroscopic behavior of the studied cement paste, based on the microscopic behavior of its constituents: cement clinker, hydrate gel, and capillary pores. The latter are referred to as material phases. The model accounts for the hierarchical organization of the microstructure across separated scales of observation, the characteristic type of interaction of the material phases located at the same hierarchical level, ellipsoidal shapes of the phases (Fig. 5), their volume fractions (Section 3.1), and their elastic and creep properties (Sections 3.2 and 3.5).

Cement paste is hierarchically organized across two scales of observation, see Fig. 5. The microstructure of a representative volume element (RVE) of the cement paste is represented as a matrix-inclusion composite, consisting of a spherical cement clinker phase embedded in a hydrate foam matrix [28]. In mature cement paste, the characteristic size of the cement clinker grains ranges from single micrometers to a few tens of micrometers. The RVE of cement paste is some three times larger [39]. Its characteristic size amounts to some 100 μm, see Fig. 5. The microstructure of an RVE of the hydrate foam is represented as a disordered "polycrystalline" arrangement of isotropically oriented hydrate gel needle phases, interacting with a spherical capillary pore phase. As for young cement pastes, hydrate gel needles, growing into the interstitial space and forming the first network of connected solid constituents, are about 100 nm wide and a few micrometers long, see Fig. 6 of [40]. The present focus, however, rests on the rather dense microstructure of mature cement pastes. It mainly contains hydrate gel needles which are several nanometers thick and some tens of nanometers long, see Fig. 8 of [40] as well as Figs. 4 and 5 of [41], and capillary pores with characteristic diameters of 25 nm [42]. The RVE of hydrate foam is some three times larger [39]. Its characteristic size amounts to some 100 nm, see Fig. 5.

3.1. Volume fractions of the constituents of cement paste

As for the cement paste, the volume fractions of the constituents are functions of the initial water-to-cement ratio, w/c, and the degree of hydration, ξ, as described by Powers' hydration model [43–45]. Relative to an RVE of cement paste (index cp), the volume fractions of the cement clinker (index cli) and the hydrate foam (index hf) read as [28]

$$f_{hf}^{cp} = \frac{20\,\xi + 63\,w/c}{20 + 63\,w/c}\,, \qquad f_{cli}^{cp} = 1 - f_{hf}^{cp}\,. \tag{11}$$

Relative to an RVE of the hydrate foam, the volume fractions of the capillary pores (index por) and the hydrate gel (index hyd) read as [28]

$$f_{hyd}^{hf} = \frac{43.15\,\xi}{20\,\xi + 63\,w/c}\,, \qquad f_{por}^{hf} = 1 - f_{hyd}^{hf}\,. \tag{12}$$

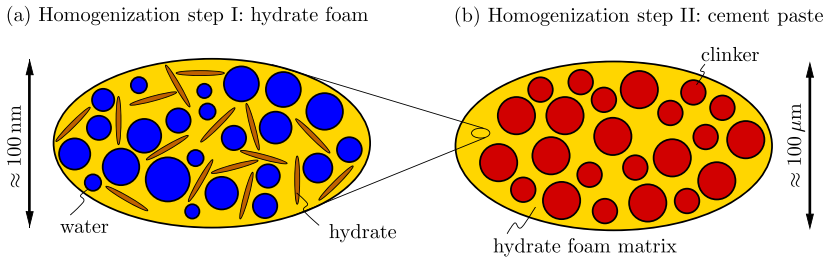

Fig. 5. Micromechanical representation of the microstructure of mature cement paste (after [28]); the two-dimensional sketches illustrate qualitative properties of three-dimensional representative volume elements (RVEs).

Table 3
Elastic bulk and shear moduli of the constituents of cement paste at 20°C.

Phase	Bulk modulus	Shear modulus	
Pores	$k_{e,por} = 0\,\text{GPa}$	$\mu_{e,por} = 0\,\text{GPa}$	[28]
Hydrate gel at 20°C	$k_{e,hyd} = 18.69\,\text{GPa}$	$\mu_{e,hyd} = 11.76\,\text{GPa}$	[28]
cement clinker	$k_{e,cli} = 116.7\,\text{GPa}$	$\mu_{e,cli} = 53.8\,\text{GPa}$	[47]

3.2. Elastic properties of the constituents of the cement paste

Because the microstructural constituents (index q) of Fig. 5 are isotropic, their elastic (index e) stiffness tensors $\mathbb{C}_q$ can be expressed e.g. in terms of the bulk moduli, $k_{e,q}$, and the shear moduli, $\mu_{e,q}$:

$$\mathbb{C}_q = 3k_{e,q}\,\mathbb{I}^{vol} + 2\mu_{e,q}\,\mathbb{I}^{dev}\,. \tag{13}$$

$\mathbb{I}^{vol}$ and $\mathbb{I}^{dev}$ are the volumetric and deviatoric parts, respectively, of the symmetric fourth-order identity tensor $\mathbb{I}$. Their components read as $I_{ijkl} = \left(\delta_{ik}\delta_{jl} + \delta_{il}\delta_{jk}\right)/2$, $I^{vol}_{ijkl} = \left(\delta_{ij}\delta_{kl}\right)/3$, and $I^{dev}_{ijkl} = I_{ijkl} - I^{vol}_{ijkl}$, where δ_{ij} is the Kronecker delta which is equal to 1 for $i = j$, and equal to 0 otherwise.

As regards the mechanical behavior of the pores and the water therein, drained conditions are considered [24,46]. This implies a vanishing elastic stiffness of the pores: $k_{e,por} = \mu_{e,por} = 0\,\text{GPa}$, see Table 3. The elastic stiffness moduli of cement clinker, $k_{e,cli}$ and $\mu_{e,cli}$, are assumed to be constant in the temperature interval from 10 to 50 °C, see Table 3 for numerical values. The elastic stiffness moduli of the hydrate gel, $k_{e,hyd}$ and $\mu_{e,hyd}$, listed in Table 3, refer to 20 °C. They decrease with increasing temperature, as will be discussed in the following paragraphs.

Molecular dynamics simulations coupled with a Grand Canonical Monte-Carlo approach by Bonnaud et al. [14] have shown that the water content of C-S-H building blocks decreases with increasing temperature. This results in both a stiffening of the building blocks and a decrease of their packing density within the C-S-H gel. Because the latter effect dominates, the C-S-H gel effectively softens with increasing temperature. These results were confirmed and extended to different calcium-to-silicon ratios by Zhang et al. [18] using a reactive molecular simulation model. The two previous studies focused on properties of C-S-H after exposure to high temperatures. Xin et al. [16], in turn, also investigated low temperatures, performing molecular dynamics simulations to study the stiffness of the C-S-H gel at specific temperatures, taken from the interval of 100 to 500 K.

The moduli reported in [14,16,18] are normalized with respect to their values at 20 °C. They are illustrated as a dimensionless function of the absolute temperature, T, see Fig. 6. Provided that a data source does not specify a stiffness value at 20 °C, it is estimated based on inter/extrapolation between/from the closest two adjacent moduli reported.

The temperature interval of interest in the present study ranges from 10 to 50 °C. As for the absolute temperature, this implies $T/(293\,\text{K}) \in [\,0.97\,,\,1.10\,]$. Within this range, the elastic stiffness of C-S-H is approximated as a linear function of the temperature, see the solid black line in Fig. 6. The slope, $\alpha = 0.46$, is equal to that of a best linear fit of the X17-data, noting that these data refer to a temperature interval containing the one of the present study at its center. The identified slope is used to model the temperature-dependence of the elastic modulus of the hydrate gel

$$\frac{E_{e,hyd}(T)}{E_{e,hyd}(293\,\text{K})} = 1 + 0.46\left(1 - \frac{T}{293\,\text{K}}\right). \tag{14}$$

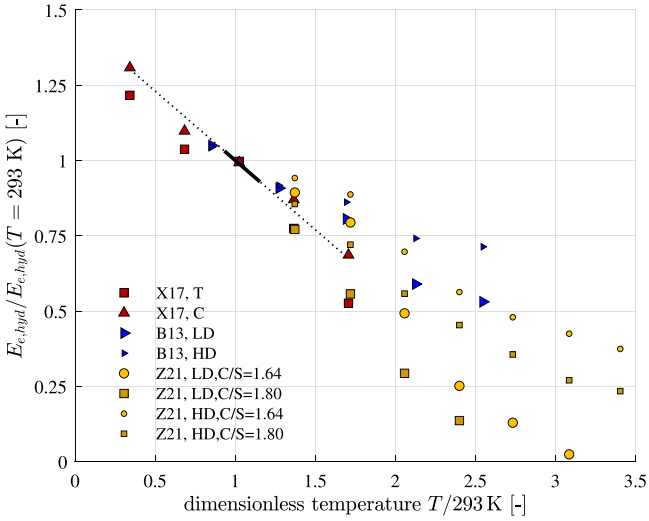

Fig. 6. Dimensionless elastic moduli of C-S-H as a function of the absolute temperature; points label results of molecular simulations: red points (X17) refer to tensile (T) and compressive (C) loading from Xin et al. [16], blue points (B13) to LD and HD C-S-H from Bonnaud et al. [14], and yellow points (Z21) to LD and HD C-S-H with different calcium-to-silica ratios (C/S) from Zhang et al. [18]; in the temperature interval of interest, the solid black line is used, see Eq. (14). (For interpretation of the references to color in this figure legend, the reader is referred to the web version of this article.)

Poisson's ratio of cementitious hydrates is virtually independent of temperature, as shown by molecular simulations of mechanically similar tobermorite (9 Å, 11 Å, and 14 Å) and jennite, see [48] and Fig. 7. The bulk and shear moduli of the hydrate gel are related to its elastic modulus and Poisson's ratio as

$$k_{e,hyd}(T) = \frac{E_{e,hyd}(T)}{3\left(1 - 2\nu_{e,hyd}\right)}, \tag{15}$$

$$\mu_{e,hyd}(T) = \frac{E_{e,hyd}(T)}{2\left(1 + \nu_{e,hyd}\right)}. \tag{16}$$

Eqs. (15) and (16) underline that the bulk and shear moduli depend on the temperature in the same linear fashion as the elastic modulus; at least in the temperature interval of interest,

$$k_{e,hyd} = 18.69\,\text{GPa} \times \left[1 + 0.46\left(1 - \frac{T}{293\,\text{K}}\right)\right], \tag{17}$$

$$\mu_{e,hyd} = 11.76\,\text{GPa} \times \left[1 + 0.46\left(1 - \frac{T}{293\,\text{K}}\right)\right], \tag{18}$$

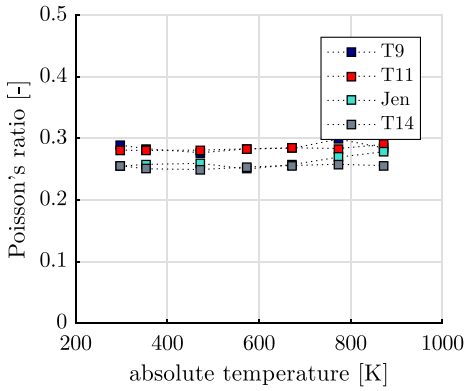

Fig. 7. Poisson's ratio of tobermorite (T9, T11, T14 Å) and jennite (Jen) as a function of the temperature [48].

where 18.69 GPa and 11.76 GPa are the values of the bulk and the shear modulus, respectively, at 20 °C, see Table 3.

3.3. Homogenization of the elastic modulus

Bottom-up homogenization from the scale of the isotropically oriented hydrate gel needles and the capillary pores to the one of the hydrate foam is performed by means of the self-consistent scheme [49,50]. This scheme requires an iterative determination of the bulk and the shear modulus of the hydrate foam, given as

$$k_{e,hf} = \frac{f_{hyd}^{hf}\, k_{e,hyd}\, A_{\infty,hyd}^{vol}}{f_{por}^{hf}\, A_{\infty,por}^{vol} + f_{hyd}^{hf}\, A_{\infty,hyd}^{vol}}, \tag{19}$$

$$\mu_{e,hf} = \frac{f_{hyd}^{hf}\, \mu_{e,hyd}\, A_{\infty,hyd}^{dev}}{f_{por}^{hf}\, A_{\infty,por}^{dev} + f_{hyd}^{hf}\, A_{\infty,hyd}^{vol}}, \tag{20}$$

where $A_{\infty,por}^{vol}$, $A_{\infty,por}^{dev}$, $A_{\infty,hyd}^{vol}$, and $A_{\infty,hyd}^{dev}$ are functions of $k_{e,hyd}$, $\mu_{e,hyd}$, $k_{e,hf}$, and $\mu_{e,hf}$, see Appendix A.

Bottom-up homogenization from the scale of the hydrate foam and the cement clinker to the one of the cement paste is performed by means of the Mori–Tanaka–Benveniste scheme [51,52]:

$$k_{e,cp} = \frac{f_{cli}^{cp}\, k_{e,cli}\left[1+\frac{3(k_{e,cli}-k_{e,hf})}{3k_{e,hf}+4\mu_{e,hf}}\right]^{-1} + f_{hf}^{cp}\, k_{e,hf}}{f_{cli}^{cp}\left[1+\frac{3(k_{e,cli}-k_{e,hf})}{3k_{e,hf}+4\mu_{e,hf}}\right]^{-1} + f_{hf}^{cp}}, \tag{21}$$

$$\mu_{e,cp} = \frac{f_{cli}^{cp}\, \mu_{e,cli}\left[1+\frac{6(k_{e,hf}+2\mu_{e,hf})(\mu_{e,cli}-\mu_{e,hf})}{5\mu_{e,hf}(3k_{e,hf}+4\mu_{e,hf})}\right]^{-1} + f_{hf}^{cp}\, \mu_{e,hf}}{f_{cli}^{cp}\left[1+\frac{6(k_{e,hf}+2\mu_{e,hf})(\mu_{e,cli}-\mu_{e,hf})}{5\mu_{e,hf}(3k_{e,hf}+4\mu_{e,hf})}\right]^{-1} + f_{hf}^{cp}}. \tag{22}$$

The elastic modulus of the cement paste follows as

$$E_{e,cp} = \frac{9\, k_{e,cp}\, \mu_{e,cp}}{3k_{e,cp} + \mu_{e,cp}}. \tag{23}$$

3.4. Comparison of model predictions with experimental results

As for the application of the multiscale model to the experimentally studied cement paste, the volume fractions according to Eqs. (11) and (12) are evaluated for the initial water-to-cement mass ratio $w/c = 0.42$. The hydration degree ξ is unknown. It is identified such that the model reproduces the experimentally determined expected value of the elastic modulus at 20 °C, $E_e = 21.3$ GPa, see Table 2. This results in $\xi = 0.80$, see Table 4 for the related volume fractions. Also the compressive strength of the specimens is unknown. It is quantified by means of a validated strength model [29]. For cement paste with $w/c = 0.42$ and $\xi = 0.80$ the model suggests a uniaxial compressive strength of 73.4 MPa, see Eqs. (24)–(28) in [29]. Thus, the maximum stress applied during creep testing reported in Section 2, i.e. $\max\sigma = 12$ MPa, is equal to 16.4% of the uniaxial compressive strength. The small degree of utilization underlines that testing was carried out in the linear creep regime [31].

Table 4
Volume fractions according to Eqs. (11) and (12), evaluated for $w/c = 0.42$ and $\xi = 0.80$.

$f_{hf}^{cp} = 0.9139$	$f_{hyd}^{hf} = 0.8125$
$f_{cli}^{cp} = 0.0861$	$f_{por}^{hf} = 0.1875$
sum = 1.0000	sum = 1.0000

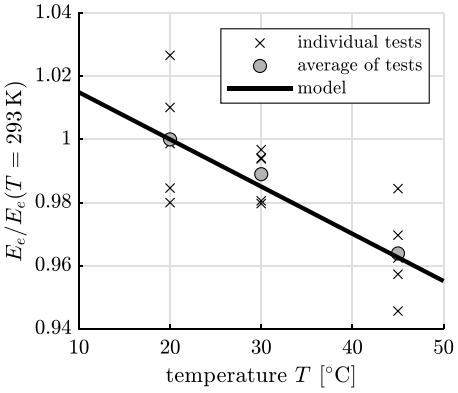

Fig. 8. Elastic modulus of the cement paste as a function of temperature: experimental results, see the crosses and the circles, and predictions of the used multiscale model, see the line.

Table 5
Creep properties of the hydrate gel.

Creep shear modulus at 20°C	$\mu_{c,hyd} = 20.93$ GPa	[24]
Power-law exponent	$\beta_{hyd} = 0.25$	[24]

Model-predicted elastic moduli of the cement paste are computed by means of Eqs. (19)–(23) for temperatures from 10 to 50 °C. Input values are volume fractions from Table 4 and phase stiffnesses from Table 3, Eq. (17), and Eq. (18). Model-predicted elastic moduli of the cement paste decrease linearly with increasing temperature and agree well with the experimental data, see Fig. 8. At 50 °C, the elastic modulus is by some 4% smaller than at 20 °C.

3.5. Creep properties of the constituents of the cement paste

The hydrate gel is the only viscoelastic material phase. Based on its elastic bulk modulus, $k_{e,hyd}$, its elastic shear modulus, $\mu_{e,hyd}$, the creep shear modulus, $\mu_{c,hyd}$, and the power-law-exponent, β_{hyd}, the creep compliance tensor reads as [24]:

$$\mathbb{J}_{hyd}(t-\tau) = \frac{1}{3k_{e,hyd}}\mathbb{I}^{vol} + \frac{1}{2}\left[\frac{1}{\mu_{e,hyd}} + \frac{1}{\mu_{c,hyd}}\left(\frac{t-\tau}{t_{ref}}\right)^{\beta_{hyd}}\right]\mathbb{I}^{dev}, \tag{24}$$

with $t_{ref} = 86400$ s, $k_{e,hyd}$ and $\mu_{e,hyd}$ given in Eqs. (17) and (18), and $\mu_{c,hyd}$ and β_{hyd} given in Table 5. The listed value of $\mu_{c,hyd}$ refers to 20 °C. It decreases with increasing temperature, as will be described next.

The influence of the temperature on the creep activity of cementitious materials is usually described by an Arrhenius law. The activation energy of the creep compliance is close to that of *unconfined* bulk water, see e.g., [9]. This suggests that macroscopic creep of cementitious materials is governed by nanoscopic mechanisms involving water as a key player [13]. Water in nanoscopic pores, however, is known to be *confined*, hence the expressions "water in a liquid crystal state", "adsorbed water", "structured water", and "glassy water" [53]. While the

absolute values of the viscosities of bulk water and of confined water are expected to be *different*, their activation energy is virtually *the same*, as demonstrated by means of molecular dynamics simulations [17]. This provides the motivation to set the activation energy equal to the one of bulk water:

$$Q_{H_2O} = 17.57\,\mathrm{kJ/mol}\,. \tag{25}$$

This value is applicable in the temperature interval from 1 to 45°C, see [54]. Thus, the Arrhenius law for the creep shear modulus reads as

$$\mu_{c,hyd} = 20.93\,\mathrm{GPa} \times \exp\left[\frac{Q_{H_2O}}{R}\left(\frac{1}{T} - \frac{1}{293\,\mathrm{K}}\right)\right], \tag{26}$$

where 20.93 GPa is the creep shear modulus at 20 °C, see Table 5, and $R = 8.314\,\mathrm{J/(mol\,K)}$ stands for the universal gas constant.

3.6. Homogenization of the creep modulus

Micro-to-macro upscaling of the temperature-dependent viscoelastic behavior is performed in the theoretical framework of linear micro-viscoelasticity [55,56], also referred to as the correspondence principle. The time-dependent problem is transformed to the Laplace–Carson (LC) space, where a series of quasi-elastic upscaling problems are solved, followed by back-transformation to the time domain, as will be described next.

The present study is focused on the viscoelastic behavior of cementitious materials under *isothermal conditions*. Thus, the temperature-dependent moduli $k_{e,hyd}$, $\mu_{e,hyd}$, and $\mu_{c,hyd}$ in Eq. (24) are constant with respect to time. The only source of microscopic time-dependence is the power-law-term of the compliance tensor of the hydrate gel, see Eq. (24).

The LC-transform $\varphi^{LC}(p)$ of any time-dependent function $\varphi(t)$ is defined as

$$\varphi^{LC}(p) = p\int_0^\infty \varphi(t)\,\exp(-pt)\,\mathrm{d}t\,, \tag{27}$$

where $p \in \mathbb{R}^+$ is the variable in the LC space [57]. The smaller p, the longer the time interval from which information of the transformed function $\varphi(t)$ is effectively conveyed to the LC space. This can be quantified in terms of the exponential function $\exp(-pt)$ in Eq. (27), which is equal to 0.998 for $pt = 0.002$ and equal to 0.002 for $pt = 6.215$. Based on these values, the time range $t \geq 0$ is subdivided into three intervals:

- $\exp(-pt)$ is equal or at least very close to 1 for all $t \in [0\,;\,\frac{0.002}{p}]$. From this time interval, virtually the full information of $\varphi(t)$ is conveyed to the LC space,
- $\exp(-pt)$ decays from almost 1 to almost 0 in the time range $t \in [\frac{0.002}{p}\,;\,\frac{6.215}{p}]$. From this interval, information of $\varphi(t)$ is partly conveyed to the LC space, and
- $\exp(-pt)$ is equal or at least very close to 0 for time instants $t \geq \frac{6.215}{p}$. From this time interval, virtually no information of $\varphi(t)$ is conveyed to the LC space, see also Fig. 9.

As for $p = 10^0$/s, the three time intervals read as: $t \in [0\,\mathrm{s}\,;\,0.002\,\mathrm{s}]$, $t \in [0.002\,\mathrm{s}\,;\,6.215\,\mathrm{s}]$, and $t > 6.215$ s. This underlines that information of $\varphi(t)$ from the first 2 ms is "fully" conveyed to the LC space and that virtually no information of $\varphi(t)$ from $t > 6$ s arrives in the LC space. The full information of the first three minutes (= 180 seconds) is conveyed to the LC space provided that the value of p has decreased to 10^{-5}/s. For this value of p, the three time intervals read as: $t \in [0\,\mathrm{s}\,;\,200\,\mathrm{s}]$, $t \in [200\,\mathrm{s}\,;\,1\,\mathrm{week}]$, and $t > 1$ week, see Fig. 9. Thus, the analysis of three-minutes creep tests will be based on values of p in the interval from 10^{+5}/s to 10^{-5}/s.

The LC-transform of the stiffness tensor of an isotropic and linear elastic phase with *time-independent* material properties, see Eq. (13), simply yields

$$\mathbb{C}_q^{LC} = 3k_{e,q}\,\mathbb{I}^{vol} + 2\mu_{e,q}\,\mathbb{I}^{dev}\,. \tag{28}$$

The LC-transform of the *time-dependent* creep compliance tensor of the hydrate gel, see Eq. (24), yields

$$\mathbb{J}_{hyd}^{LC}(p) = \frac{1}{3k_{e,hyd}}\mathbb{I}^{vol} + \frac{1}{2\mu_{hyd}^{LC}(p)}\mathbb{I}^{dev}\,, \tag{29}$$

with

$$\frac{1}{2\mu_{hyd}^{LC}(p)} = \frac{1}{2\mu_{e,hyd}} + \frac{\Gamma\left(\beta_{hyd}+1\right)}{2\mu_{c,hyd}}\left(\frac{1}{t_{ref}\,p}\right)^{\beta_{hyd}}\,, \tag{30}$$

where $\Gamma(\beta_{hyd}+1)$ denotes the gamma function evaluated for $\beta_{hyd}+1 = 1.25$. Inversion of $\mathbb{J}_{hyd}^{LC}(p)$ yields the LC-transformed stiffness tensor of the hydrate gel as

$$\mathbb{C}_{hyd}^{LC}(p) = 3k_{e,hyd}\,\mathbb{I}^{vol} + 2\mu_{hyd}^{LC}(p)\,\mathbb{I}^{dev}\,. \tag{31}$$

Eqs. (28) and (31) underline that a viscoelastic homogenization problem manifests itself in the LC space as a (quasi-)elastic upscaling challenge. It has to be met for different values of the LC variable p.

Bottom-up homogenization from the scale of the isotropically oriented hydrate gel needles and the capillary pores to the one of the hydrate foam is performed based on Eqs. (19), (20), (A.1), and (A.2). Therein, $k_{e,hf}$ is replaced by $k_{hf}^{LC}(p)$, $\mu_{e,hf}$ by $\mu_{hf}^{LC}(p)$, and $\mu_{e,hyd}$ by $\mu_{hyd}^{LC}(p)$.

Bottom-up homogenization from the scale of the hydrate foam and the cement clinker to the one of the cement paste is performed based on Eqs. (21) and (22). Therein, $k_{e,cp}$ is replaced by $k_{cp}^{LC}(p)$, $\mu_{e,cp}$ by $\mu_{cp}^{LC}(p)$, $k_{e,hf}$ by $k_{hf}^{LC}(p)$, and $\mu_{e,hf}$ by $\mu_{hf}^{LC}(p)$. The corresponding LC-transformed solution for the uniaxial creep compliance reads as

$$J_{cp}^{LC}(p) = \frac{3k_{cp}^{LC}(p) + \mu_{cp}^{LC}(p)}{9\,k_{cp}^{LC}(p)\,\mu_{cp}^{LC}(p)}\,. \tag{32}$$

$J_{cp}^{LC}(p)$ is evaluated for a cement paste with $w/c = 0.42$ and $\xi = 0.80$, at a specific absolute temperature T, and for values of p, spanning over 10 orders of magnitude, namely, from 10^{+5}/s to 10^{-5}/s. The p-dependent part of $J_{cp}^{LC}(p)$ is obtained by subtracting the elastic compliance, $1/E_{e,cp}$. Thereby, $E_{e,cp}$ is taken from Eq. (23). Illustrating $J_{cp}^{LC}(p) - 1/E_{e,cp}$ as a function of p in a double logarithmic diagram underlines that the p-dependent homogenization results in the LC space follow a virtually linear trend, the slope of which amounts to −0.25, see Fig. 10. Thus, homogenization results in the LC space can be approximated based on the function

$$J_{cp}^{LC}(p) \approx \frac{1}{E_{e,cp}} + \frac{\Gamma\left(\beta_{cp}+1\right)}{E_{c,cp}}\left(\frac{1}{t_{ref}\,p}\right)^{\beta_{cp}}\,, \tag{33}$$

with $\beta_{cp} = 0.25$. This allows for identification of $E_{c,cp}$. The function (33) can be analytically back-transformed to the time domain, yielding

$$J_{cp}(t-\tau) = \frac{1}{E_{e,cp}} + \frac{1}{E_{c,cp}}\left(\frac{t-\tau}{t_{ref}}\right)^{\beta_{cp}}\,. \tag{34}$$

Thus, the microscopic power-law creep behavior of the hydrate gel needles manifests itself macroscopically as a power-law creep behavior of the cement paste, with the same power-law exponent: $\beta_{cp} = \beta_{hyd}$.

3.7. Comparison of model predictions with experimental results

As for the application of the multiscale model to the experimentally studied cement paste, the volume fractions are taken from Table 4. The macroscopic creep modulus of the cement paste is computed for temperatures taken from the interval from 10 to 50 °C. The model-predictions agree well with the experimental data, see Fig. 11. At 50 °C, the creep modulus is by some 48% smaller than at 20 °C, i.e. the creep activity at 50 °C is virtually twice as large as that at 20 °C.

The model-predicted strain evolutions also agree well with the experimental results, compare the dashed lines with the solid lines in Fig. 12. The residual error between the predicted strain evolutions,

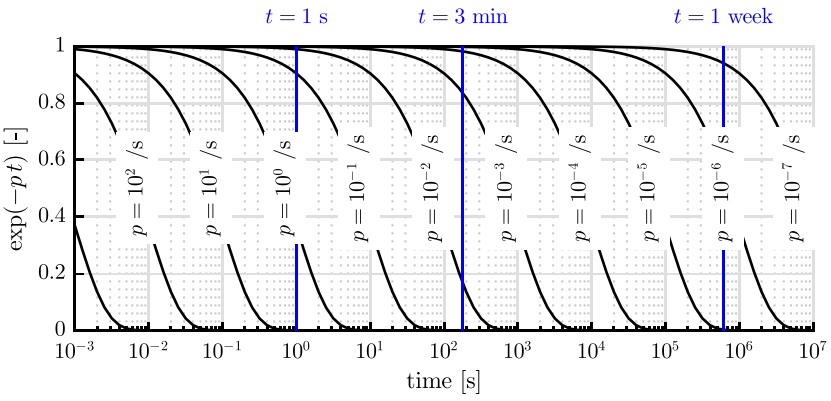

Fig. 9. Graphs of the exponential function $\exp(-pt)$ for different orders of magnitude of the LC variable p.

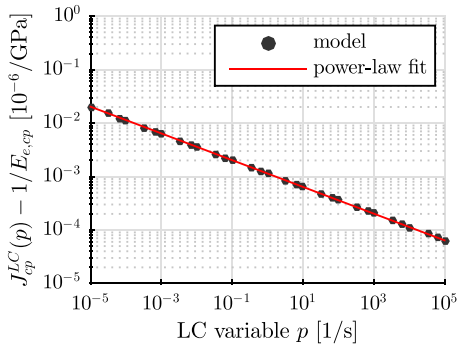

Fig. 10. LC-transformed solution for the p-dependent part of the homogenized creep compliance function of a cement paste with w/c = 0.42 and ξ = 0.80, at 20 °C, as a function of the LC-variable p, spanning over 10 orders of magnitude, namely, from 10^{+5}/s to 10^{-5}/s.

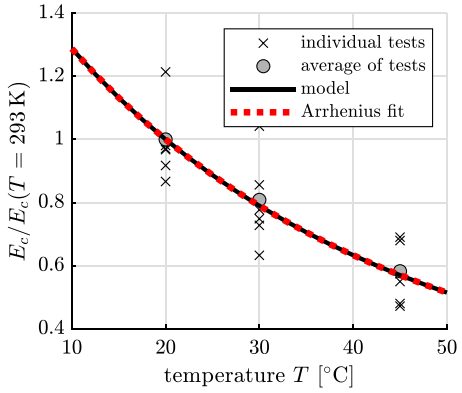

Fig. 11. Creep modulus of the cement paste as a function of temperature: experimental results, see the crosses and circles, predictions of the used multiscale model, see the black solid line, and best macroscopic Arrhenius fit, see the dashed red line.

$\varepsilon_{mod}(t)$, and the measured strain evolutions, $\varepsilon(t)$, see Eq. (2), is defined as

$$\epsilon = \frac{1}{n}\sum_{i=1}^{n}\left|\varepsilon_{mod}(t_i) - \varepsilon(t_i)\right| , \tag{35}$$

with n = 1000 referring to 1000 equidistant time instants within the investigated interval, ranging from zero to t_{lap} + 180 s. The prediction errors amount to 1.5×10^{-6}, 1.3×10^{-6}, and 8.0×10^{-6}, for 20 °C, 30 °C, and 45 °C, respectively.

4. Discussion

4.1. Origin of temperature-dependence of the stiffness moduli of the hydrate gel

In the investigated interval of temperatures ranging from 20 to 45 °C, irreversible microstructural changes (= thermal degradation of cement paste) have unlikely taken place. Instead, there are two reversible processes that have occurred. They are likely responsible for the temperature-dependence of the elastic modulus as described by Eq. (14) and illustrated in Fig. 8.

- Increasing the temperature of any solid results in an intensified disordered motion of the atoms. It goes along with the reversible increase of the average distance between them. This process manifests itself macroscopically by "thermal expansion" [19]. Because of the increased average distance, less force is required to push the atoms closer to each other, compared to the situation at the reference temperature. This results in a slightly decreasing elastic stiffness [19].
- Increasing the temperature of calcium-silicate-hydrates leads to quasi-instantaneous water migration from the interlayer spaces to the surrounding pores. This process was predicted by molecular simulations [14,16,18] as well as by multiscale poromechanical modeling of the anomalous thermal expansion behavior of mature cement paste [42]. Experimental evidence was obtained by means of proton nuclear magnetic resonance relaxometry [58]. This change in the composition of calcium-silicate-hydrates is likely to exert an influence on their elastic stiffness.

It is expected that the two described phenomena exert an influence on the creep modulus of the hydrates, with changes of the same order of magnitude as the ones of the elastic stiffness, see Fig. 8. However, they are by one order of magnitude smaller than the decrease of the creep modulus. This follows from the decrease of the viscosity of water, induced by an increase of temperature, as described by Eq. (26) and illustrated in Fig. 11. Thus, processes which likely govern the temperature-dependence of the elastic modulus appear to have less influence on the temperature-dependence of the creep modulus, at least for the temperature range investigated herein.

4.2. Activation energy of the homogenized creep modulus of the cement paste

The upscaled creep modulus of the cement paste is used to quantify the macroscopic activation energy Q_{cp} occurring in the following equation:

$$\frac{1}{E_{c,cp}(T)} = \frac{1}{E_{c,cp}(293\,\mathrm{K})}\exp\left[-\frac{Q_{cp}}{R}\left(\frac{1}{T}-\frac{1}{293\,\mathrm{K}}\right)\right], \tag{36}$$

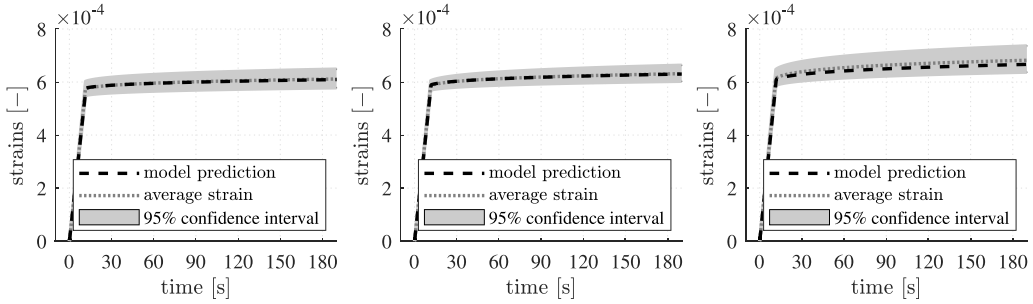

Fig. 12. Comparison of model-predicted strains, see the black dashed lines, with experimentally measured strains, see the gray solid lines; the shaded domains represent the 95% confidence interval of the experimentally measured strains, see Section 2.2.

The optimal value of Q_{cp} amounts to 17.57 kJ/mol, see the red dashed line in Fig. 11. This underlines that the value of the activation energy of the creep modulus is *the same* at the microscopic scale of the hydrate gel needles and at the macroscopic scale of the cement paste, see also Eq. (25). This result can be explained based on the analysis of microstresses experienced by the hydrate foam and the cement clinker, respectively.

4.3. Effectiveness of stress redistributions from creeping to non-creeping constituents of the cement paste

A three-minutes creep test is simulated, using the multiscale model. The test is idealized, given that the uniaxial stress state

$$\boldsymbol{\sigma}_{cp} = \sigma_{zz,cp}\, \mathbf{e}_z \otimes \mathbf{e}_z \tag{37}$$

is imposed *instantaneously* (= step-wise loading) onto a sample of cement paste with a temperature amounting to 20 °C. The volume-averaged stresses experienced immediately after application of the loading by the hydrate foam and the cement clinker, respectively, can be computed based on the *elastic* stress downscaling relation

$$\boldsymbol{\sigma}_q = \left(B_q^{vol}\, \mathbb{I}^{vol} + B_q^{dev}\, \mathbb{I}^{dev} \right) : \boldsymbol{\sigma}_{cp}\,, \qquad q = [\,hf\,, cli\,]\,, \tag{38}$$

with the following volumetric and deviatoric components of the stress downscaling tensors of the hydrate foam matrix,

$$B_{hf}^{vol} = \left[f_{hf}^{cp} + f_{cli}^{cp} \frac{k_{e,cli}}{k_{e,hf}} \left(\frac{3k_{e,hf} + 4\mu_{e,hf}}{3k_{e,cli} + 4\mu_{e,hf}} \right) \right]^{-1}, \tag{39}$$

$$B_{hf}^{dev} = \left[f_{hf}^{cp} + f_{cli}^{cp} \frac{\mu_{e,cli}}{\mu_{e,hf}} \times \left(\frac{5\,\mu_{e,hf}(3k_{e,hf} + 4\mu_{e,hf})}{\mu_{e,hf}(8\mu_{e,hf} + 9k_{e,hf}) + 6\,\mu_{e,cli}\,(2\mu_{e,hf} + k_{e,hf})} \right) \right]^{-1}, \tag{40}$$

and of the cement clinker inclusions [59],

$$B_{cli}^{vol} = \left[\frac{k_{e,hf}}{k_{e,cli}} f_{hf}^{cp} \left(1 - \frac{3k_{e,hf}}{3k_{e,hf} + 4\mu_{e,hf}} \right) + \left(f_{cli}^{cp} + f_{hf}^{cp} \frac{3k_{e,hf}}{3k_{e,hf} + 4\mu_{e,hf}} \right) \right]^{-1}, \tag{41}$$

$$B_{cli}^{dev} = \left[\frac{\mu_{e,hf}}{\mu_{e,cli}} f_{hf}^{cp} \left(1 - \frac{6(k_{e,hf} + 2\mu_{e,hf})}{5(3k_{e,hf} + 4\mu_{e,hf})} \right) + \left(f_{cli}^{cp} + f_{hf}^{cp} \frac{6(k_{e,hf} + 2\mu_{e,hf})}{5(3k_{e,hf} + 4\mu_{e,hf})} \right) \right]^{-1}. \tag{42}$$

Evaluation of the Eqs. (37)–(42) for the studied cement paste yields

$$\sigma_{zz,hf} = 0.939\, \sigma_{zz,cp}\,, \tag{43}$$

$$\sigma_{zz,cli} = 1.647\, \sigma_{zz,cp}\,. \tag{44}$$

At the time-invariant macroscopic stress state of Eq. (37) the microstrain of the hydrate foam increases with time because of creep of the hydrate gel needles at the next smaller scale of observation. One would expect that progressively increasing deformations of the viscoelastic hydrate foam tend to redistribute microstresses from the hydrate foam to the elastic (= non-creeping) cement clinker. However, the cement clinker particles are embedded in and supported by the hydrate foam matrix, see Fig. 5. This renders redistributions of *phase-volume-averaged* microstresses ineffective. Consequently, the volume-averaged microstresses of both the hydrate foam and the cement clinker are virtually constant. This can be quantified by computing, in the LC space, the evolution of their volume-averaged microstresses. To this end, $k_{e,hf}$ is replaced by $k_{hf}^{LC}(p)$ and $\mu_{e,hf}$ by $\mu_{hf}^{LC}(p)$ in Eqs. (38)–(42). The LC-transformed solutions are computed for values of p, spanning over 10 orders of magnitude: from 10^{+5}/s to 10^{-5}/s. The obtained LC-transformed volume-averaged axial normal stresses of the two microstructural constituents are normalized with respect to the axial macrostress imposed on the cement paste, see the dots in Fig. 13. The red solid lines in this figure refer to the elastic stress downscaling solutions of Eqs. (43) and (44). Fig. 13 underlines that the *volume-averaged* microstresses of the hydrate foam matrix and of the cement clinker inclusions are virtually constant throughout the studied creep test. Notably, this does not imply that stress states are also virtually constant at specific points of the microstructure.

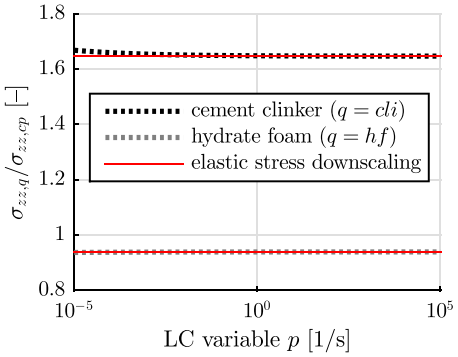

Fig. 13. Evolution of the volume-averaged normal stress components (aligned with the direction of macroscopic loading) of the hydrate foam and the cement clinker in a uniaxial creep test of cement paste (w/c = 0.42 and ξ = 0.80), subjected to the macrostress state of Eq. (37), at 20 °C, as a function of the LC-variable p, spanning over 10 orders of magnitude: from 10^{+5}/s to 10^{-5}/s; the red lines refer to the elastic solutions of the stress downscaling problem, see Eqs. (43) and (44).

Time-invariant volume-averaged microstresses of cement clinker go along with time-invariant volume-averaged strains. The strain average rule relates the progressively increasing macrostrain $\boldsymbol{\varepsilon}_{cp}$ of the cement paste to the progressively increasing volume-averaged microstrain $\boldsymbol{\varepsilon}_{hf}$ of the hydrate foam and to the time-invariant volume-averaged

microstrain $\boldsymbol{\varepsilon}_{cli}$ of the cement clinker, i.e.

$$\boldsymbol{\varepsilon}_{cp}(t) = f_{hf}^{cp}\,\boldsymbol{\varepsilon}_{hf}(t) + f_{cli}^{cp}\,\boldsymbol{\varepsilon}_{cli}\,. \tag{45}$$

The functional arguments, indicating a dependence on time t, underline that the evolution of the macroscopic creep strain of the cement paste is affine to the evolution of the microscopic volume-averaged creep strain of the hydrate foam. Therefore, also the creep kinetics of the hydrate foam are affine to those of the cement paste.

For the sake of completeness, ineffective redistributions of phase-volume-averaged stresses are also discussed at the next smaller scale of observation referring to the microstructure of the hydrate foam. The latter is subjected, on average, to a time-invariant stress state, see Fig. 13. The microstrains of the creeping hydrate gel needles increase with time. Again, no significant stress-redistribution takes place, because (i) the capillary pores cannot take over any share of the load and (ii) all hydrate gel needles share the same linear viscoelastic behavior. Thus, the stresses experienced by the hydrate gel needle phases, oriented in specific directions, are on average also virtually constant. This implies that the creep kinetics of the hydrate gel needles are affine to those of the hydrate foam.

Summarizing, it is a direct consequence of the morphology of the microstructure of the cement paste that microstructural stress redistributions are on average ineffective. This means that temperature-driven changes of the hydrates' creep shear modulus, $\mu_{c,hyd}$, as described by the Arrhenius law of Eq. (26), lead to very similar changes of the homogenized creep modulus of the cement paste.

4.4. Multiscale analysis of cement pastes with different compositions and maturities

In the following, it will be demonstrated that the described results also hold for cement pastes with different initial water-to-cement mass ratios and hydration degrees. The corresponding sensitivity analysis refers to 17 different values of w/c, ranging from 0.20 in steps of 0.05 to 1.00, and to 18 different values of ξ, ranging from 0.05 in steps of 0.05 to 0.90. Creep moduli of 284 different cement pastes, see Table 6, are homogenized for 9 different temperatures ranging from 10 °C in steps of 5 °C to 50 °C. Thus, a total of 2556 homogenized creep moduli are computed. In order to illustrate the influence of the temperature, the values $E_c(T, w/c, \xi)$ are illustrated in a normalized fashion, see Fig. 14 where the ordinate refers to $E_c(T, w/c, \xi)/E_c(T = 293\text{K}, w/c, \xi)$, i.e., the 2556 computed values of the creep moduli are normalized with respect to the values of the creep moduli obtained with *the same* composition and maturity, obtained at 20°C. The 2556 computed points, referring to a great variety of initial compositions and maturity, see Table 6, are located in the immediate vicinity of the Arrhenius law of Eq. (36), evaluated for $Q_{cp} = Q_{H_2O} = 17.57\,\text{kJ/mol}$, see the dashed line in Fig. 14. This demonstrates that neither the investigated scale of observation, nor the initial water-to-cement ratio (w/c) or maturity (ξ) alter the temperature activation behavior of the creep compliance of ordinary Portland cement pastes. The temperature activation law for the creep modulus of the cement paste reads as

$$E_c(T) = E_c(20\ ^\circ\text{C}) \times \exp\left[\frac{Q_{H_2O}}{R}\left(\frac{1}{T} - \frac{1}{293.15\,\text{K}}\right)\right]. \tag{46}$$

4.5. Implications for the activation energy of the homogenized creep moduli of mortars and concretes

Mortars and concretes are matrix-inclusion composites. Aggregates and sand are embedded, as inclusions, into a cement paste matrix. The latter is a creeping material phase, while the inclusions are non-creeping (purely elastic) constituents. This situation is reminiscent of the microstructure of cement paste, consisting of non-creeping inclusions in a creeping matrix. Thus, it may be expected that stress redistributions inside the concrete, from the creeping cement paste matrix to the non-creeping aggregates and the sand, are also ineffective. This is particularly the case during three-minutes creep tests, but also for longer-term loading as will be discussed in Section 4.6.

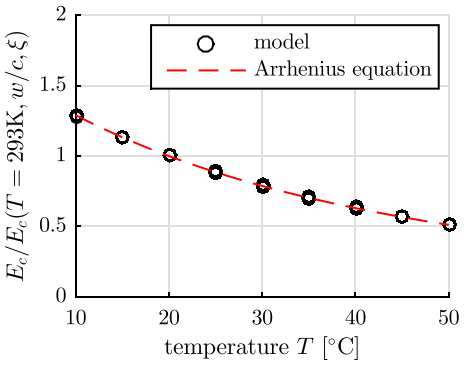

Fig. 14. Normalized homogenized creep moduli of 284 different cement pastes (for values of w/c and ξ see Table 6) obtained at 9 specific temperatures ranging from 10 °C in steps of 5 °C to 50 °C: the 2556 ordinate values refer to $E_c(T, w/c, \xi)/E_c(T = 293\,\text{K}, w/c, \xi)$, see the text for details.

Aggregates and sand usually constitute 60 to 70% of the volume of concrete. The remaining 40 to 30% of the volume are occupied by cement paste. Thus, the volume fraction of the non-creeping inclusions is larger than that of the creeping matrix. This is different from the microstructure of mature cement paste, where the volume fraction of the non-creeping cement clinker inclusions is smaller than that of the creeping hydrate foam matrix, see e.g. numerical values of f_{hf}^{cp} and f_{cli}^{cp} in Table 4. Still, in the sensitivity analysis presented in the preceding subsection, it was shown that creep-induced stress redistributions are insignificant also for $w/c = 0.20$ and $\xi = 0.10$. These properties refer to a microstructure of the cement paste, the volume of which is occupied to some 55% by the non-creeping clinker grains. Only the approximately remaining 45% of the volume are occupied by the creeping hydrate foam matrix. These volume fractions are comparable to those of concrete, see the beginning of this paragraph. Thus, the microstructure of concrete is both qualitatively and quantitatively similar to that of the cement paste, for which the microscopic stresses in the creeping matrix and in the non-creeping inclusions were shown to be virtually constant. This supports the expectation that creep-induced stress redistributions are ineffective also within the microstructure of concrete and that the activation energy of the viscosity of water is not only relevant to the creep moduli of the hydrate gel, the hydrate foam, and cement paste, but also to the creep moduli of mortar and concrete. And indeed, activation energies, suitable for explaining many experimental data regarding creep of concrete with different compositions, amount e.g. to 16.0 kJ/mol [1,60] and 16.6 kJ/mol [9]. These values are close to the ones observed herein and, thus, also close to the one of liquid water.

4.6. Longer-term stress redistributions

In order to provide insight into stress redistributions during creep tests which last much longer than the ones in the present study, the LC-transformed solutions are back-transformed to the time domain using the Gaver–Wynn–Rho algorithm [61,62], see Fig. 15. Within the first month after loading, the average stress experienced by the clinker grains only increases slightly, while the average stress experienced by the hydrate foam decreases unnoticeably. The difference between the absolute values of the stress changes can be explained based on the stress average rule,

$$\boldsymbol{\sigma}_{cp} = f_{hf}^{cp}\,\boldsymbol{\sigma}_{hf}(t) + f_{cli}^{cp}\,\boldsymbol{\sigma}_{cli}(t)\,, \tag{47}$$

considering of the volume fractions of Table 4. The larger change of the average stress experienced by clinker, multiplied by the relatively small

Table 6
Initial compositions and maturities of cement pastes analyzed by means of the developed multiscale model, see the cells marked with an "x", empty cells refer to substoichiometric initial compositions and hydration degrees larger than the maximum attainable hydration degree: $\max \xi = \frac{w/c}{0.42}$, see e.g. [28].

w/c =	0.20	0.25	0.30	0.35	0.40	0.45	0.50	0.55	0.60	0.65	0.70	0.75	0.80	0.85	0.90	0.95	1.00
$\xi = 0.05$	x	x	x	x	x	x	x	x	x	x	x	x	x	x	x	x	x
$\xi = 0.10$	x	x	x	x	x	x	x	x	x	x	x	x	x	x	x	x	x
$\xi = 0.15$	x	x	x	x	x	x	x	x	x	x	x	x	x	x	x	x	x
$\xi = 0.20$	x	x	x	x	x	x	x	x	x	x	x	x	x	x	x	x	x
$\xi = 0.25$	x	x	x	x	x	x	x	x	x	x	x	x	x	x	x	x	x
$\xi = 0.30$	x	x	x	x	x	x	x	x	x	x	x	x	x	x	x	x	x
$\xi = 0.35$	x	x	x	x	x	x	x	x	x	x	x	x	x	x	x	x	x
$\xi = 0.40$	x	x	x	x	x	x	x	x	x	x	x	x	x	x	x	x	x
$\xi = 0.45$	x	x	x	x	x	x	x	x	x	x	x	x	x	x	x	x	x
$\xi = 0.50$		x	x	x	x	x	x	x	x	x	x	x	x	x	x	x	x
$\xi = 0.55$		x	x	x	x	x	x	x	x	x	x	x	x	x	x	x	x
$\xi = 0.60$			x	x	x	x	x	x	x	x	x	x	x	x	x	x	x
$\xi = 0.65$			x	x	x	x	x	x	x	x	x	x	x	x	x	x	x
$\xi = 0.70$			x	x	x	x	x	x	x	x	x	x	x	x	x	x	x
$\xi = 0.75$				x	x	x	x	x	x	x	x	x	x	x	x	x	x
$\xi = 0.80$				x	x	x	x	x	x	x	x	x	x	x	x	x	x
$\xi = 0.85$					x	x	x	x	x	x	x	x	x	x	x	x	x
$\xi = 0.90$					x	x	x	x	x	x	x	x	x	x	x	x	x

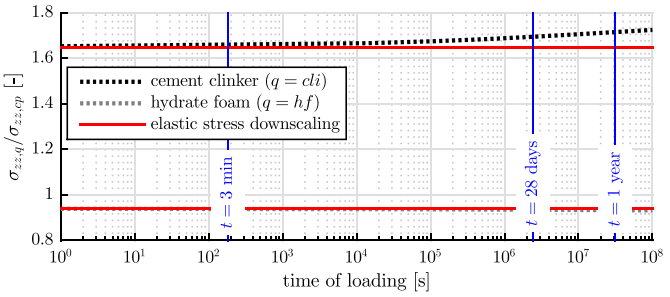

Fig. 15. Time-evolution of the normal stress components (aligned with the direction of macroscopic loading) of the hydrate foam (gray data points) and of the cement clinker (black data points) in a uniaxial creep test of cement paste according to Eq. (37): $w/c = 0.42$, $\xi = 0.80$, and $T = 20$ °C.

volume fraction, is equal to the smaller change of the average stress experienced by the hydrate foam, multiplied by the relatively large volume fraction. The increase of the average clinker stress becomes noticeable some 3 h after the start of the creep tests, see $t \approx 10^4$ s in Fig. 15. Concerning creep predictions for even longer time periods, it is important to note that power-law creep of cementitious materials (as assumed herein for multiscale modeling) is only valid for creep test durations up to some 1 or 2 months. Thereafter, a transition to logarithmic creep takes place [20]. Logarithmic creep kinetics can be upscaled from minutes-long microindentation tests [63]. Having performed such tests at different temperatures, ranging from 10 to 60 °C, in a laboratory, conditioned to a relative humidity of 30%, it was found that the contact creep modulus is virtually constant, see [64]. However, both long-term creep and partial saturation are beyond the scope of this paper.

4.7. Nanoindentation study of DeJong and Ulm [65]

DeJong and Ulm [65] studied the decrease of the elastic stiffness moduli of calcium-silicate-hydrates (C-S-H), resulting from an increase of temperature, by means of grid nanoindentation of cement pastes at material ages of 28 days. Each specimen was first heated to a specific temperature between 25 and 700 °C, then cooled, followed by grid nanoindentation at 200 positions. Testing after the return to room temperature renders the direct comparability with the present study (testing at elevated temperature) questionable. Still, it is interesting to discuss characteristic sizes associated with nanoindentation testing and to compare them with the characteristic sizes of the microstructure of mature cement paste, discussed in the second paragraph of Section 3, see also Fig. 5. The indentation depths amounted to some 200 nm [65]. Thus, the radius of the probed domain and the size of the characterized RVEs amounted to some 4 μm and to some 100 nm, respectively [66]. This underlines that nanoindentation-derived stiffness values refer to the hydrate foam (see Fig. 5) rather than to the hydrate gel.

5. Conclusions

Based on results obtained from testing in the range of temperatures from 20 °C to 45 °C and from modeling in the range of temperatures from 10 °C to 50 °C, the following conclusions are drawn:

- For the precise evaluation of quasi-static uniaxial compression tests it is essential to separate the elastic and the creep parts during the whole test. It must be considered that both instantaneous elastic and time-dependent creep deformations are measured during the short initial phase of loading. 2.9% to 7.1% of the total strains that have developed during the loading phase were creep strains, see Fig. B.16.
- Assuming that (i) the strains measured during loading were elastic and (ii) the creep strains developed exclusively during the three-minutes load plateau would result in an overestimation of the elastic strains by 3.0% to 7.6%. This would lead to considerable inaccuracies of the identified values of the elastic moduli as well as to an underestimation of the creep strains by 34%, which would result in significant inaccuracies of the identified values of the creep moduli.
- The elastic modulus of mature cement paste decreases by 1.0% and 3.6% if the temperature increases from 20 °C to 30 °C and 45 °C, respectively.
- The creep modulus decreases by 17% and 45% if the temperature increases from 20 °C to 30 °C and 45 °C, respectively.
- Homogenized elastic and creep moduli agree well with the experimental results. This corroborates the possibility of micro-to-macro upscaling, based on published molecular simulation results concerning the temperature-dependent elastic stiffness of the hydration products and the temperature activation of the viscosity of water, respectively.
- The morphology of the microstructure of the cement paste (elastic cement clinker particles embedded in a hydrate foam matrix, and isotropically oriented hydrate gel needles, directly interacting with capillary pores) renders microstructural stress redistribution from creeping hydrates to non-creeping clinker grains ineffective. This is particularly the case during three-minutes creep tests

performed in the present study, but also for longer-term durations of constant loading of up to a few weeks (= the range of validity of the power-law creep kinetics analyzed herein).
- Time-invariant macroscopic loading leads to virtually constant microstresses, experienced by the creeping hydrates for loading durations of up to a few weeks, see Fig. 15. Therefore, the macroscopic measurable creep kinetics of cement paste is virtually equal to the one of microscopic hydration products.
- Results from multiscale modeling suggest that the Arrhenius-type activation energy of the creep modulus of cementitious materials is virtually independent of the scale, the composition, and the maturity. It may be set equal to the activation energy of bulk and confined water [17]. This was experimentally verified for one composition, tested at mature age.

The presented experimental study was limited to a maximum temperature of 45 °C and focused on mature samples of water-saturated cement paste ($w/c = 0.42$), subjected to three-minutes creep tests at some 16% of the uniaxial compressive strength of the material. This leaves several interesting topics for future studies. The latter may cover e.g. different initial compositions, early age material testing, partial saturation, longer creep test durations, higher degrees of utilization, and repeated testing at the reference temperature after an exposure to elevated temperature, in order to assess potential damage induced by the heating and cooling cycle.

List of symbols and abbreviations

A	Cross-sectional area of specimen
A_∞	Component of Eshelby-problem-related strain downscaling tensor
B	Component of stress downscaling tensor
$\mathbb{C}$	Stiffness tensor
C-S-H	Calcium-silicate-hydrates
c	Index, standing for "creep"
cli	Index, standing for "cement clinker"
cp	Index, standing for "cement paste"
d	Diameter of specimen
dev	Index, standing for "deviatoric part"
e	Index, standing for "elastic"
E_c	Creep modulus
E_e	Elastic modulus
E_i	Statistical variable
$\mathbf{e}_z$	Unit vector in the z-direction
F	Axial force
f	Volume fraction
H_2O	Index, standing for "water"
h	Height of specimen
hf	Index, standing for "hydrate foam"
hyd	Index, standing for "hydrate gel"
$\mathbb{I}$	Symmetric fourth-order identity tensor
I_{ijkl}	$ijkl$-th component of $\mathbb{I}$
$\mathbb{J}$	Creep compliance tensor
J	Uniaxial creep function
k	Bulk modulus
LC	Laplace-Carson
LVDTs	Linear Variable Displacement Transducers
m	Mass of specimen
m_i	Expected value of the natural logarithm of the statistical variable
mod	Index, standing for "modeling"
n	Number of time steps
P	Quantile of the statistical variable
PDF	Probability density function
p	Variable in the LC space
por	Index, standing for "capillary pores"
Q	Activation energy
R	Universal gas constant
RVE	Representative volume element
s_i	Standard deviation of the natural logarithm of the statistical variable
T	Absolute temperature
t	Time variable
t_{ref}	Reference time
t_{lap}	Time instant, marking the end of the load application process
w/c	Initial water-to-cement mass ratio
vol	Index, standing for "volumetric part"
z	Cartesian coordinate
α	Slope of the linear regression function
β	Power-law exponent
$\Delta\ell_i$	Change of length of LVDT ($i = 1, 2, 3, 4, 5$)
δ_{ij}	Kronecker delta
ϵ	Residual error
ε	Axial strain component
$\boldsymbol{\varepsilon}$	Strain tensor
Γ	Gamma function
μ	Shear modulus
ν	Poisson's ratio
σ	Axial stress component
$\dot{\sigma}$	Rate of σ
$\boldsymbol{\sigma}$	Stress tensor
σ_{lap}	Normal stress, marking the beginning of the load plateau
τ	Time-like integration variable
$\varphi(t)$	Time-dependent function
$\varphi^{LC}(p)$	LC-transform of $\varphi(t)$
ξ	Degree of hydration

CRediT authorship contribution statement

Eva Binder: Investigation, Methodology, Formal analysis, Software, Validation, Visualization, Writing – original draft, Writing – review & editing. **Markus Königsberger:** Formal analysis, Methodology, Investigation, Software, Validation, Visualization, Writing – original draft, Funding acquisition, Writing – review & editing. **Rodrigo Díaz Flores:** Formal analysis, Methodology, Investigation, Software, Visualization, Writing – review & editing. **Herbert A. Mang:** Writing – review & editing, Funding acquisition. **Christian Hellmich:** Conceptualization, Methodology, Writing – review & editing. **Bernhard L.A. Pichler:** Conceptualization, Methodology, Supervision, Writing – review & editing, Project administration.

Declaration of competing interest

The authors declare that they have no known competing financial interests or personal relationships that could have appeared to influence the work reported in this paper.

Data availability

Data will be made available on request.

Acknowledgments

Financial support by the Austrian Science Fund (FWF), provided within project P 281 31-N32 "Bridging the Gap by Means of Multiscale Structural Analyses", and the Belgian National Funds for Scientific Research (FNRS), as well as support of the experiments, provided by Wolfgang Dörner, Dr. Olaf Lahayne, and Dr. Roland Reihsner, are gratefully acknowledged.

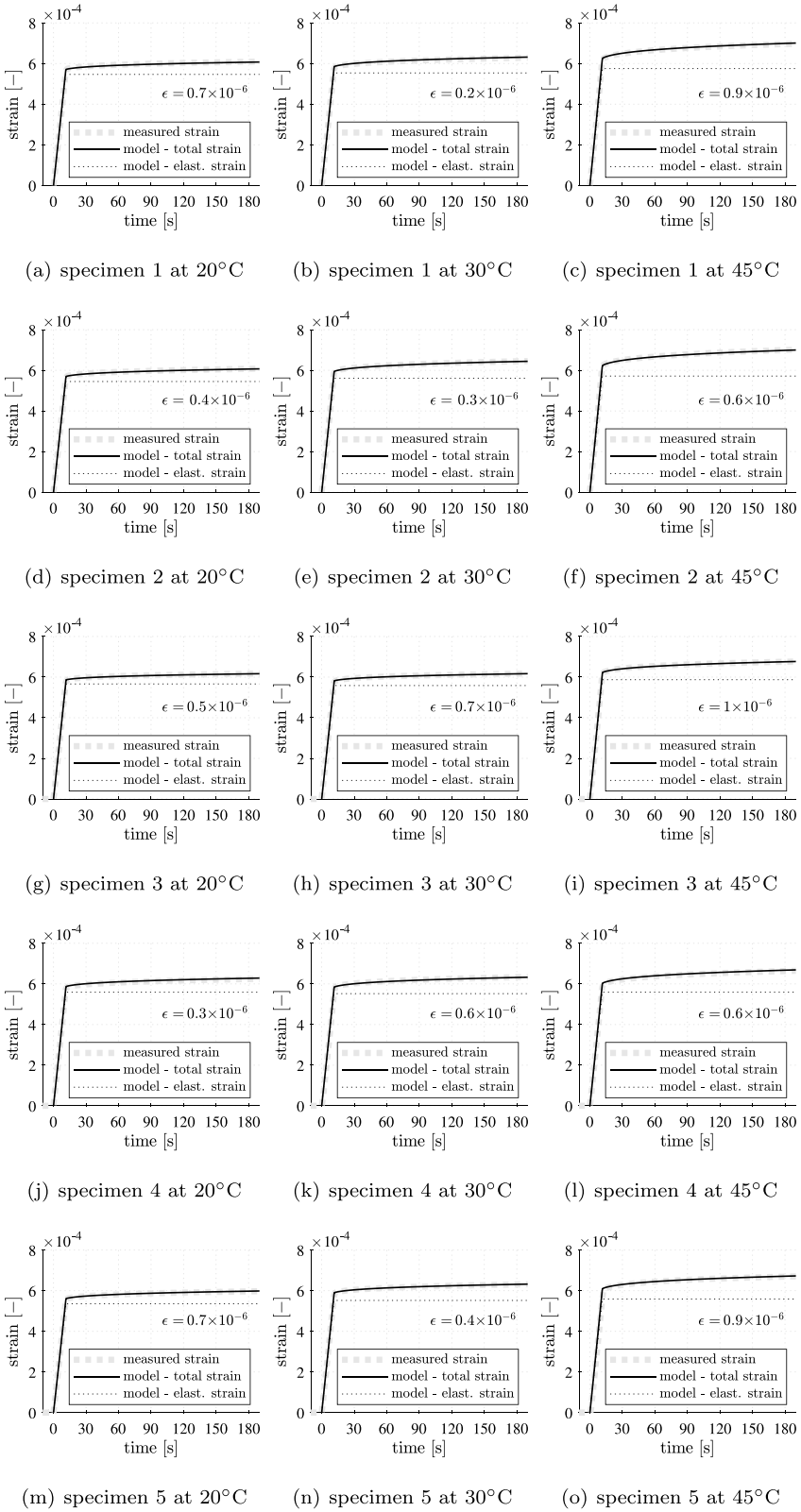

(a) specimen 1 at 20°C (b) specimen 1 at 30°C (c) specimen 1 at 45°C

(d) specimen 2 at 20°C (e) specimen 2 at 30°C (f) specimen 2 at 45°C

(g) specimen 3 at 20°C (h) specimen 3 at 30°C (i) specimen 3 at 45°C

(j) specimen 4 at 20°C (k) specimen 4 at 30°C (l) specimen 4 at 45°C

(m) specimen 5 at 20°C (n) specimen 5 at 30°C (o) specimen 5 at 45°C

Fig. B.16. Strain histories of the 15 creep tests: the gray dashed lines refer to measurements, the black solid lines to Eqs. (6) and (7), see Table 2 for the identified values of the elastic modulus and the creep modulus, respectively, ϵ denotes the residual error between the measured and the modeled strain histories according to Eq. (35).

Appendix A. Homogenization of isotropic properties of the hydrate foam

The quantities $A^{vol}_{\infty,por}$ and $A^{dev}_{\infty,por}$ as well as $A^{vol}_{\infty,hyd}$ and $A^{dev}_{\infty,hyd}$, which are part of the Eqs. (19) and (20), read as [24]

$$A^{vol}_{\infty,por} = \left[1 - \frac{3\,k_{e,hf}}{3\,k_{e,hf} + 4\,\mu_{e,hf}}\right]^{-1},$$
$$A^{dev}_{\infty,por} = \left[1 - \frac{6}{5}\frac{k_{e,hf} + 2\,\mu_{e,hf}}{3\,k_{e,hf} + 4\,\mu_{e,hf}}\right]^{-1}, \tag{A.1}$$

and

$$A^{vol}_{\infty,hyd} = \frac{3\,k_{e,hf} + \mu_{e,hyd} + 3\,\mu_{e,hf}}{3\,k_{e,hyd} + \mu_{e,hyd} + 3\,\mu_{e,hf}},$$
$$\begin{aligned} A^{dev}_{\infty,hyd} = \Big\{ & 9\,k_{e,hyd}\left[\mu_{e,hyd}\right]^2 k_{e,hf} + 64\left[\mu_{e,hf}\right]^4 + \\ & \left[63\,k_{e,hyd} + 84\,k_{e,hf} + 184\,\mu_{e,hyd}\right]\left[\mu_{e,hf}\right]^3 + \\ & \left[156\,k_{e,hyd}\,\mu_{e,hyd} + 120\,k_{e,hf}\,\mu_{e,hyd}\right. \\ & \left. +72\left[\mu_{e,hyd}\right]^2 + 81\,k_{e,hyd}\,k_{e,hf}\right]\left[\mu_{e,hf}\right]^2 + \\ & \left[36\,k_{e,hf}\left[\mu_{e,hyd}\right]^2 + 21\,k_{e,hyd}\left[\mu_{e,hyd}\right]^2\right. \\ & \left. +90\,k_{e,hf}\,k_{e,hyd}\,\mu_{e,hyd}\right]\mu_{e,hf}\Big\} \\ & \Big(5\left\{\left[\mu_{e,hf}\right]^2 + \left[7\,\mu_{e,hyd} + 3\,k_{e,hf}\right]\mu_{e,hf} + 3\,k_{e,hf}\,\mu_{e,hyd}\right\} \\ & \left[\mu_{e,hf} + \mu_{e,hyd}\right]\left[3\,k_{e,hyd} + \mu_{e,hyd} + 3\,\mu_{e,hf}\right]\Big)^{-1}. \end{aligned} \tag{A.2}$$

Appendix B. Identification of the elastic and creep moduli from strain evolutions measured in the 15 creep tests

See Fig. B.16.

References

[1] T. Vidal, A. Sellier, W. Ladaoui, X. Bourbon, Effect of temperature on the basic creep of high-performance concretes heated between 20 and 80°C, J. Mater. Civ. Eng. 27 (7) (2015) B4014002.

[2] J.B. Odelson, E.A. Kerr, W. Vichit-Vadakan, Young's modulus of cement paste at elevated temperatures, Cem. Concr. Res. 37 (2) (2007) 258–263.

[3] J. Salençon, Handbook of Continuum Mechanics – General Concepts. Thermoelasticity, Springer, Berlin, 2001.

[4] K.W. Nasser, A.M. Neville, Creep of old concrete at normal and elevated temperatures, ACI J. Proc. 64 (2) (1967) 97–103.

[5] T. Hannant, Strain behaviour of concrete up to 95°C under compressive stresses, in: Proceedings of the Conference on Prestressed Concrete Pressure Vessels, Group C, Institution of Civil Engineers, 1967, pp. 57–71.

[6] R. Browne, Properties of concrete in reactor vessels, in: Prestressed Concrete Pressure Vessels, Thomas Telford Publishing, 1968, pp. 131–151.

[7] K. Nasser, H. Marzouk, Creep of concrete at temperatures from 70 to 450 F under atmospheric pressure, ACI J. 78 (13) (1981) 147–150.

[8] G. Kommendant, M. Polivka, D. Pirtz, Study of concrete properties for prestressed concrete reactor vessels, final report-part II, creep and strength characteristics of concrete at elevated temperatures, in: Rep. No. UCSESM 76-3 Prepared for General Atomic Company, 1976, pp. 55–81.

[9] W. Ladaoui, T. Vidal, A. Sellier, X. Bourbon, Effect of a temperature change from 20 to 50°C on the basic creep of HPC and HPFRC, Mater. Struct. 44 (9) (2011) 1629–1639.

[10] A. Sellier, S. Multon, L. Buffo-Lacarrière, T. Vidal, X. Bourbon, G. Camps, Concrete creep modelling for structural applications: non-linearity, multi-axiality, hydration, temperature and drying effects, Cem. Concr. Res. 79 (2016) 301–315.

[11] B. Tamtsia, J. Beaudoin, Basic creep of hardened cement paste: A re-examination of the role of water, Cem. Concr. Res. 30 (9) (2000) 1465–1475.

[12] P. Acker, F.-J. Ulm, Creep and shrinkage of concrete: physical origins and practical measurements, Nucl. Eng. Des. 203 (2–3) (2001) 143–158.

[13] A.A. Al-Manaseer, M.A. Chiorino, M.A. Issa, K.A. Rieder, Z.P. Bazant, M.A. Daye, H. Marzouk, I. Robertson, J.J. Brooks, W.H. Dilger, et al., Report on factors affecting shrinkage and creep of hardened concrete, Concr. Int. 21 (2005).

[14] P.A. Bonnaud, Q. Ji, K.J. Van Vliet, Effects of elevated temperature on the structure and properties of calcium-silicate-hydrate gels: The role of confined water, Soft Matter 9 (28) (2013) 6418–6429.

[15] R.K. Mishra, A.K. Mohamed, D. Geissbühler, H. Manzano, T. Jamil, R. Shahsavari, A.G. Kalinichev, S. Galmarini, L. Tao, H. Heinz, et al., Cemff: A force field database for cementitious materials including validations, applications and opportunities, Cem. Concr. Res. 102 (2017) 68–89.

[16] H. Xin, W. Lin, J. Fu, W. Li, Z. Wang, Temperature effects on tensile and compressive mechanical behaviors of CSH structure via atomic simulation, J. Nanomater. 2017 (2017) 8476258.

[17] A. Zaragoza, M.A. Gonzalez, L. Joly, I. López-Montero, M.A. Canales, A.L. Benavides, C. Valeriani, Molecular dynamics study of nanoconfined TIP4P/2005 water: how confinement and temperature affect diffusion and viscosity, Phys. Chem. Chem. Phys. 21 (25) (2019) 13653–13667.

[18] Y. Zhang, Q. Zhou, J.W. Ju, M. Bauchy, New insights into the mechanism governing the elasticity of calcium silicate hydrate gels exposed to high temperature: A molecular dynamics study, Cem. Concr. Res. 141 (2021) 106333.

[19] D.A. Padmavathi, Potential energy curves & material properties, Mater. Sci. Appl. 2 (2011) 97–104.

[20] M. Irfan-ul Hassan, M. Königsberger, R. Reihsner, C. Hellmich, B. Pichler, How water-aggregate interactions affect concrete creep: Multiscale analysis, J. Nanomech. Micromech. 7 (4) (2017) 04017019.

[21] L. Göbel, A. Osburg, B. Pichler, The mechanical performance of polymer-modified cement pastes at early ages: Ultra-short non-aging compression tests and multiscale homogenization, Constr. Build. Mater. 173 (2018) 495–507.

[22] M. Ausweger, E. Binder, O. Lahayne, R. Reihsner, G. Maier, M. Peyerl, B. Pichler, Early-age evolution of strength, stiffness, and non-aging creep of concretes: Experimental characterization and correlation analysis, Materials 12 (2) (2019) 207.

[23] Y. Gan, M. Vandamme, Y. Chen, E. Schlangen, K. van Breugel, B. Šavija, Experimental investigation of the short-term creep recovery of hardened cement paste at micrometre length scale, Cem. Concr. Res. 149 (2021) 106562.

[24] M. Königsberger, M. Irfan-ul Hassan, B. Pichler, C. Hellmich, Downscaling based identification of nonaging power-law creep of cement hydrates, J. Eng. Mech. 142 (12) (2016) 04016106.

[25] M. Königsberger, T. Honório, J. Sanahuja, B. Delsaute, B.L.A. Pichler, Homogenization of nonaging basic creep of cementitious materials: A multiscale modeling benchmark, Constr. Build. Mater. 290 (2021) 123144.

[26] P. Karte, M. Hlobil, R. Reihsner, W. Dörner, O. Lahayne, J. Eberhardsteiner, B. Pichler, Unloading-based stiffness characterisation of cement pastes during the second, third and fourth day after production, Strain 51 (2) (2015) 156–169.

[27] M. Irfan-ul Hassan, B. Pichler, R. Reihsner, C. Hellmich, Elastic and creep properties of young cement paste, as determined from hourly repeated minute-long quasi-static tests, Cem. Concr. Res. 82 (2016) 36–49.

[28] B. Pichler, C. Hellmich, Upscaling quasi-brittle strength of cement paste and mortar: A multi-scale engineering mechanics model, Cem. Concr. Res. 41 (5) (2011) 467–476.

[29] B. Pichler, C. Hellmich, J. Eberhardsteiner, J. Wasserbauer, P. Termkhajornkit, R. Barbarulo, G. Chanvillard, Effect of gel–space ratio and microstructure on strength of hydrating cementitious materials: An engineering micromechanics approach, Cem. Concr. Res. 45 (2013) 55–68.

[30] P. Rossi, J.-L. Tailhan, F. Le Maou, L. Gaillet, E. Martin, Basic creep behavior of concretes investigation of the physical mechanisms by using acoustic emission, Cem. Concr. Res. 42 (1) (2012) 61–73.

[31] M.F. Ruiz, A. Muttoni, P.G. Gambarova, Relationship between nonlinear creep and cracking of concrete under uniaxial compression, J. Adv. Concr. Technol. 5 (3) (2007) 383–393.

[32] M.E. Gurtin, E. Sternberg, On the linear theory of viscoelasticity, Arch. Ration. Mech. Anal. 11 (1) (1962) 291–356.

[33] L. Boltzmann, Zur Theorie der elastischen Nachwirkung [On the theory of the elastic aftereffect], Ann. Der Physik 241 (11) (1878) 430–432, In German.

[34] B.T. Tamtsia, J.J. Beaudoin, J. Marchand, The early age short-term creep of hardening cement paste: load-induced hydration effects, Cem. Concr. Compos. 26 (5) (2004) 481–489.

[35] O. Coussy, Poromechanics, John Wiley & Sons, 2004.

[36] L. Göbel, A. Osburg, B. Pichler, The mechanical performance of polymer-modified cement pastes at early ages: Ultra-short non-aging compression tests and multiscale homogenization, Constr. Build. Mater. 173 (2018) 495–507.

[37] L. Göbel, M. Königsberger, A. Osburg, B. Pichler, Viscoelastic behavior of polymer-modified cement pastes: Insight from downscaling short-term macroscopic creep tests by means of multiscale modeling, Appl. Sci. 8 (4) (2018) 487.

[38] P. Dohnalík, B.L.A. Pichler, L. Zelaya-Lainez, O. Lahayne, G. Richard, C. Hellmich, Micromechanics of dental cement paste, J. Mech. Behav. Biomed. Mater. 124 (2021) 104863.

[39] W.J. Drugan, J.R. Willis, A micromechanics-based nonlocal constitutive equation and estimates of representative volume element size for elastic composites, J. Mech. Phys. Solids 44 (4) (1996) 497–524.

[40] I. Richardson, Tobermorite/jennite-and tobermorite/calcium hydroxide-based models for the structure of C-S-H: applicability to hardened pastes of tricalcium silicate, β-dicalcium silicate, Portland cement, and blends of Portland cement with blast-furnace slag, metakaolin, or silica fume, Cem. Concr. Res. 34 (9) (2004) 1733–1777.

[41] R. Taylor, I. Richardson, R. Brydson, Nature of C–S–H in 20 year old neat ordinary Portland cement and 10% Portland cement–90% ground granulated blast furnace slag pastes, Adv. Appl. Ceram. 106 (6) (2007) 294–301.
[42] H. Wang, C. Hellmich, Y. Yuan, H. Mang, B. Pichler, May reversible water uptake/release by hydrates explain the thermal expansion of cement paste? – arguments from an inverse multiscale analysis, Cem. Concr. Res. 113 (2018) 13–26.
[43] T. Powers, T. Brownyard, Studies of the physical properties of hardened Portland cement paste, Am. Concrete Inst. J. Proc. 18 (2–8) (1946–1947) 101–992.
[44] T.C. Hansen, Physical structure of hardened cement paste. a classical approach, Mater. Struct. 19 (6) (1986) 423–436.
[45] P. Acker, Micromechanical analysis of creep and shrinkage mechanisms, in: Creep, Shrinkage and Durability Mechanics of Concrete and Other Quasi-Brittle Materials, Cambridge, MA, 2001, pp. 15–25.
[46] M. Königsberger, B. Pichler, C. Hellmich, Multiscale poro-elasticity of densifying calcium-silicate hydrates in cement paste: an experimentally validated continuum micromechanics approach, Internat. J. Engrg. Sci. 147 (2020) 103196.
[47] K. Velez, S. Maximilien, D. Damidot, G. Fantozzi, F. Sorrentino, Determination by nanoindentation of elastic modulus and hardness of pure constituents of Portland cement clinker, Cem. Concr. Res. 31 (4) (2001) 555–561.
[48] X.F. Wang, T.R. Li, P. Wei, D.W. Li, N.X. Han, F. Xing, Y. Gan, Z. Chen, Computational study of the nanoscale mechanical properties of C-S-H composites under different temperatures, Comput. Mater. Sci. 146 (2018) 42–53.
[49] A.V. Hershey, The elasticity of an isotropic aggregate of anisotropic cubic crystals, J. Appl. Mech. 21 (1954) 236.
[50] E. Kröner, Bounds for effective elastic moduli of disordered materials, J. Mech. Phys. Solids 25 (2) (1977) 137–155.
[51] T. Mori, K. Tanaka, Average stress in matrix and average elastic energy of materials with misfitting inclusions, Acta Metall. 21 (5) (1973) 571–574.
[52] Y. Benveniste, A new approach to the application of Mori-Tanaka's theory in composite materials, Mech. Mater. 6 (2) (1987) 147–157.
[53] T.G. Lombardo, N. Giovambattista, P.G. Debenedetti, Structural and mechanical properties of glassy water in nanoscale confinement, Faraday Discuss. 141 (2009) 359–376.
[54] R. Mills, Self-diffusion in normal and heavy water in the range 1–45.deg, J. Phys. Chem. 77 (5) (1973) 685–688.
[55] W. Read Jr., Stress analysis for compressible viscoelastic materials, J. Appl. Phys. 21 (7) (1950) 671–674.
[56] N. Laws, R. McLaughlin, Self-consistent estimates for the viscoelastic creep compliances of composite materials, Proc. R. Soc. London A: Math. Phys. Eng. Sci. 359 (1697) (1978) 251–273.
[57] C. Donolato, Analytical and numerical inversion of the Laplace–Carson transform by a differential method, Comput. Phys. Comm. 145 (2) (2002) 298–309.
[58] M. Wyrzykowski, P.J. McDonald, K.L. Scrivener, P. Lura, Water redistribution within the microstructure of cementitious materials due to temperature changes studied with ^{1}H NMR, J. Phys. Chem. C 121 (50) (2017) 27950–27962.
[59] M. Königsberger, B. Pichler, C. Hellmich, Micromechanics of ITZ–aggregate interaction in concrete Part I: stress concentration, J. Am. Ceram. Soc. 97 (2) (2014) 535–542.
[60] A.B. Hauggaard, L. Damkilde, P.F. Hansen, Transitional thermal creep of early age concrete, J. Eng. Mech. 125 (4) (1999) 458–465.
[61] D.P. Gaver Jr., Observing stochastic processes, and approximate transform inversion, Oper. Res. 14 (3) (1966) 444–459.
[62] S. Scheiner, C. Hellmich, Continuum microviscoelasticity model for aging basic creep of early-age concrete, J. Eng. Mech. 135 (4) (2009) 307–323.
[63] Q. Zhang, R. Le Roy, M. Vandamme, B. Zuber, Long-term creep properties of cementitious materials: Comparing microindentation testing with macroscopic uniaxial compressive testing, Cem. Concr. Res. 58 (2014) 89–98.
[64] J. Frech-Baronet, L. Sorelli, Z. Chen, A closer look at the temperature effect on basic creep of cement pastes by microindentation, Constr. Build. Mater. 258 (2020) 119455.
[65] M.J. DeJong, F.-J. Ulm, The nanogranular behavior of CSH at elevated temperatures (up to 700 C), Cem. Concr. Res. 37 (1) (2007) 1–12.
[66] M. Königsberger, L. Zelaya-Lainez, O. Lahayne, B.L.A. Pichler, C. Hellmich, Nanoindentation-probed Oliver-Pharr half-spaces in alkali-activated slag-fly ash pastes: Multimethod identification of microelasticity and hardness, Mech. Adv. Mater. Struct. (2021) 1–12.